ACS APPLIED MATERIALS & INTERFACES

Research Article

www.acsami.org

# Ultralong $In_2S_3$ Nanotubes on Graphene Substrate with Enhanced Electrocatalytic Activity

Sheng-qi Guo,[†] Xue Chen,[†] Fang-zhong Hu,[*,‡] Qi-chun Zhang,[*,§,∥] and Lu Liu[*,†]

[†]Tianjin Key Laboratory of Environmental Remediation and Pollution Control, College of Environmental Science and Engineering, Nankai University, Tianjin 300071, China

[‡]State Key Laboratory and Institute of Elemento-Organic Chemistry, Nankai University, Tianjin 300071, China

[§]School of Materials Science and Engineering, Nanyang Technological University, Singapore 639798, Singapore

[∥]Division of Chemistry and Biological Chemistry, School of Physical and Mathematical Sciences, Nanyang Technological University, Singapore 637371, Singapore

Supporting Information

**ABSTRACT:** Ultralong one-dimensional (1D) nanostructures including nanowires or nanotubes have been extensively studied because of their widespread applications in many fields. Although a lot of methods have been reported to prepare $In_2S_3$ nanotubes, approaching these nanotubes through one-pot solution synthesis is still extremely difficult, probably because of the intrinsic isotropic crystal growth characteristic of $In_2S_3$. In this article, we demonstrated a self-assembly approach for hydrothermal synthesis of $In_2S_3$ nanotubes/graphene composites, which contain ultralong (up to 10 $\mu$m) $In_2S_3$ nanotubes on graphene substrate. The influence of several important synthetic parameters on the final products has been systematically investigated. Importantly, the as-prepared $In_2S_3$ nanotubes/graphene composites can be easily cast on FTO to form a film, which can be used as a counter electrode. Our research indicates that the as-fabricated counter electrode exhibits excellent electrocatalytic activity toward the iodide species ($I^-/I_3^-$) reduction reaction and very high energy conversion efficiency (8.01%) in dye-sensitized solar cells.

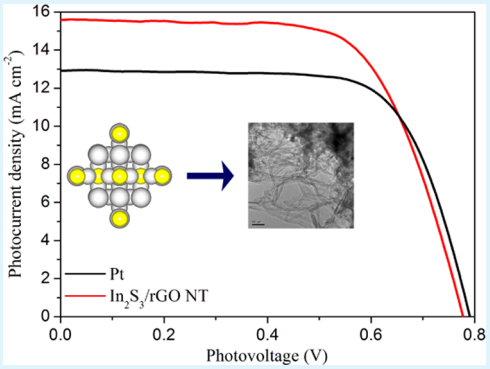


**KEYWORDS:** *$In_2S_3$, nanotube, graphene, electrocatalytic activity, dye-sensitized solar cells*

## INTRODUCTION

Indium sulfide ($In_2S_3$) is a fascinating material and has attracted intensive research enthusiasm for its excellent chemical stability and high photoconductivity.[1−3] Compared with bulky $In_2S_3$, nanoscale or low-dimensional $In_2S_3$ materials are more promising as effective REDOX catalysts not only because of their superior electron transport and slow charge recombination of electrons, which is important to facilitate charge collection, but also because of their high surface-to-volume ratio and could be effectively made into flexible substrates. Especially, nanotube (NT) structures, which are easier to be handled in device fabrication, can act as excellent channels for electron transport. Unfortunately, directly growing single-crystal $In_2S_3$ NT with high aspect ratio and large void space is extremely difficult because of the intrinsic isotropic crystal growth characteristic of $In_2S_3$. So far, although several groups have reported a variety of $In_2S_3$ nanocrystals with different morphologies,[4−9] research on the direct synthesis of $In_2S_3$ NTs is rare.[10,11]

On the other hand, many NT structures do not have enough specific surface area to capture electrons from the redox couples; thus, redox couples are very difficult to be reduced.[12] To address this issue, realizing larger specific surface areas in the $In_2S_3$-catalystic system is highly desirable because a large specific surface area normally provides more catalytic activity sites.[13] Considering these facts, one of the perfect models for $In_2S_3$ catalysts is to integrate large surface area and NT structure factor into a single unit. Over the past few years, constructing graphene/semiconductor composite has been proved to be a feasible method to increase specific surface area and conductivity because graphene has unique physical properties including large specific surface area, high Fermi velocity, and structural flexibility, which make it an ideal auxiliary substrate material.[14−17] Meanwhile, compared to a single component, composite components such as transition metal compound/graphene have shown improved physical and chemical properties due to the synergistic effects.[18−21] In 2012, the Jiang group found that freshly prepared RGO−$In_2S_3$ composite as an anode material could exhibit the enhanced cycle ability and specific capacity for lithium storage.[22] Soon after, the Xu group reported another $In_2S_3$−graphene nanocomposite, which exhibits better photocatalytic activity toward

Received: June 22, 2015
Accepted: August 26, 2015
Published: August 26, 2015

  

DOI: 10.1021/acsami.5b05519
ACS Appl. Mater. Interfaces 2015, 7, 20164−20169

selective reduction of nitroaromatic compounds in water than bare $In_2S_3$ nanoparticles.[23] Recently, the Lee group synthesized graphene/$In_2S_3$ nanoparticle composites, which also show high performance when it used as anode materials for lithium ion battery.[24] To date, although a variety of $In_2S_3$/graphene composites have been realized, the composites of NT-like $In_2S_3$/graphene have not been reported.

Herein, we report a novel self-assembly approach to fabricate a novel composite with ultralong $In_2S_3$ NTs on reduced graphene oxide ($In_2S_3$/rGO NT) under hydrothermal conditions. The influence of several important synthetic parameters on the final products is systematically investigated. Furthermore, their attractive electrocatalytic activity toward the iodide species ($I^-/I_3^-$) reduction reaction is strongly studied. More importantly, a counter electrode (CE) fabricated through the assembly of these NT composite exhibits excellent energy conversion efficiency ($\eta$) (8.01%) in dye-sensitized solar cells (DSCs), significantly higher than that of commercial Pt-CE (7.18%).

## EXPERIMENTAL SECTION

**Synthesis of Graphene Oxide (GO).** All reagents were purchased commercially (analytic grade) and were used without further purification. GO was prepared through modified Hummers method.[25] Details of the process are as follows. 2.0 g of graphite powder was dispersed into 100 mL of $H_2SO_4$ (98%) at 0 °C. Then 6.0 g of $KMnO_4$ powder was added into $H_2SO_4$ slowly, and the mixtre was continuously agitated at 35 °C for 3 days. Afterward, 200 mL of distilled water was added into the solution, and the mixture was kept at 98 °C for 2 h. When the solution was cooled to 60 °C, 10 mL of 30% $H_2O_2$ was injected into it to completely react with the excess $KMnO_4$. Bright yellow flocculent suspended solids were obtained. The suspended solids were centrifuged and washed with 30% HCl and distilled water several times, until the pH value was close to 7. The as-prepared GO was collected and kept in distilled water.

**Synthesis of $In_2S_3$/rGO NT Composites.** The $In_2S_3$/rGO NT composites were synthesized by one step of hydrothermal treatments. 0.007 g of as-prepared GO, 0.05 g of thioacetamide, 0.2 g of $InCl_3$, and 0.05 g of polyvinyl alcohol (PVA) were dispersed or dissolved in 25 mL of distilled water under continuous stirring for 30 min. The mixture was sealed in a 30 mL Teflon reactor and maintained at 180 °C for 24 h. The deep yellow power was then collected from solution, washed with ethanol, and distilled water several times and dried in air at 50 °C for 1 h.

**Preparation of Pure $In_2S_3$.** The pure $In_2S_3$ was prepared in the same way as that for $In_2S_3$/rGO NT composites but without adding any GO.

**Characterization.** The X-ray diffraction (XRD) patterns of the samples were recorded with Rigaku D/max2500 diffraction system with Cu K$\alpha$ source ($\lambda$ = 1.540 56 Å). The scanning electron microscopy (SEM) images were characterized by a Nova Nano SEM 230 field emission scanning electron microscope. The transmission electron microscopy (TEM) images were taken with a Tecnai $G^2$F20 TEM. The X-ray photoelectron spectroscopy was implemented by Kratos Axis Ultra DLD XPS. Fourier transform infrared spectroscopy (FT-IR) was carried out with American Nicolet Instrument Co. NEXUS-870 FT-IR instrument. Atomic force microscopy (AFM) was carried with Multimode8, Bruker. The mass of the electrode was recorded using a Mettler-Toledo XS105 DualRange instrument. Cyclic voltammetry (CV) was recorded with a three-electrode system on a ZAHNER ZENNIUM CIMPS-1 electrochemical workstation at a scan rate of 25 mV $s^{-1}$ (Pt was used as the counter electrode, and $Ag/Ag^+$ was used as the reference electrode). An argon-purged solution of 0.1 M $LiClO_4$, 10 mM LiI, and 1.0 mM $I_2$ in acetonitrile served as the electrolyte. Electrochemical impedance spectroscopy (EIS) of the CEs was also recorded by ZAHNER ZENNIUM CIMPS-1 electrochemical workstation, executed on dummy cells with a symmetric sandwich-like structure, CE/electrolyte/CE. The frequency range was varied from 0.1 to $10^6$ Hz. The photocurrent−voltage ($J$−$V$) curves were measured on a Keithley 2410 digital source meter under solar simulator (AM 1.5 illumination, 100 mW $cm^{-2}$), which was calibrated by a Si reference cell beforehand. All the tests were measured at room temperature.

**Cell Assembly.** 0.1 g $In_2S_3$-based powder was dispersed in 1 mL of 2.5% PEG20000 solution, stirred 30 min to obtain $In_2S_3$-based paste. The paste was sprayed onto the FTO glass substrate (LOF, TEC-15, 15 W per square) according to the doctor-blade method.[26] Then calcination was performed at 400 °C for 1 h under argon to get $In_2S_3$-based CEs. To obtain photoanode, a commercial $TiO_2$ sol (Solaronix, Ti-Nanoxide T/SP) was used to print the $TiO_2$ film on FTO. The film was immersed in an N-719 dye in ethanol for 24 h. DSCs cells were assembled by clipping two electrodes together with a spacer between the dye-sensitized $TiO_2$ electrode and the CE. The active area of cell was 0.25 $cm^2$. The liquid electrolyte was composed of 0.05 M $I_2$, 0.1 M LiI, 0.6 M 1,2-dimethyl-3-propylimidazolium iodide (DMPII), and 0.5 M 4-*tert*-butylpyridine with acetonitrile as the solvent[27] and injected into the spacer between two electrodes. Note: In the whole process of the photovoltaic tests, the use of mask or sunglasses is essential.

## RESULTS AND DISCUSSION

In the synthesis of $In_2S_3$/rGO NT hybrid nanocomposites, indium chloride ($InCl_3$), thioacetamide (TAA), polyvinyl alcohol (PVA), and graphene oxide were dispersed or dissolved in deionized water to form a homogeneous solution. After that, the mixture was transferred to a Teflon reactor and heated to 180 °C for 24 h. GO was synthesized by a modified Hummers method first. The AFM images reveal the thickness of the GO sheets to be 0.35−1 nm (Figure S1 in Supporting Information), which suggests that the GO sheets are either single or double layer. The chemical composition of the as-obtained composites was characterized by XRD, and the result is shown in Figure 1.

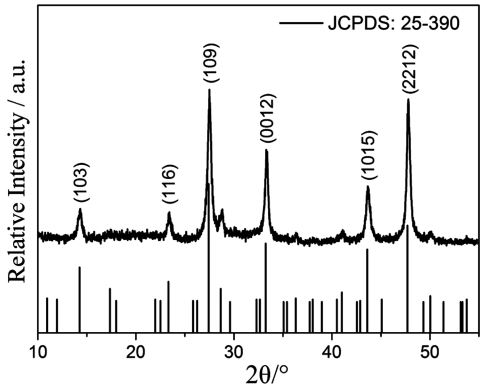


**Figure 1.** XRD pattern of the synthetic of $In_2S_3$/rGO NT sample.

XRD analysis confirmed the presence of tetragonal $In_2S_3$ with space group $I41/amd$ ($a$ = $b$ = 7.619 Å, $c$ = 32.329 Å, JCPDS 25-390). The detailed information on the as-prepared $In_2S_3$ sample can be further obtained from XPS analysis (Figure S2a). In Figure S2b, two peaks located at 444.8 and 452.6 eV are attributed to the 3d region of In atoms. The S 2p peak appeared at 162.2 eV, which can be split into two peaks at 161.7 eV for S $2p_{3/2}$ and 164.2 eV for S 2p transition, respectively (Figure S2c). This suggests that at least two kinds of sulfur species are present near the surface of the $In_2S_3$. The observed binding energies for In 3d and S 2p are similar to those reported data in other $In_2S_3$.[22,28] Moreover, the ratio of In to S is approximately 1:1.49, indicating the high purity of the product.

A panoramic view reveals that the as-prepared sample consists entirely of uniform one-dimensional (1D) structures


DOI: 10.1021/acsami.5b05519
ACS Appl. Mater. Interfaces 2015, 7, 20164−20169

(Figure 2a and Figure S3) and the diameter of each 1D structure is around 10−15 nm, growing directly on graphene

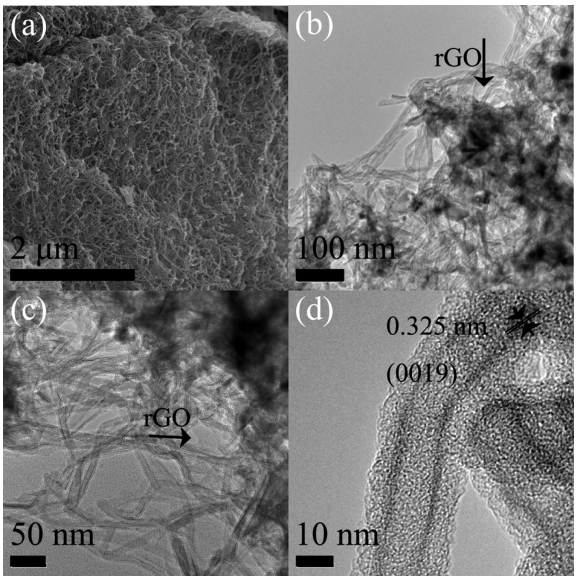


**Figure 2.** (a) FESEM image of $In_2S_3$/rGO NT sample. (b, c) TEM images of $In_2S_3$/rGO NT sample. (d) HRTEM image of $In_2S_3$/rGO NT sample.

sheet. Further examination by TEM reveals that these 1D structures possess an obvious hollow structure (Figure 2b and Figure 2c). Similar to the SEM images, a high uniformity of the nanotubes (the length up to 10 $\mu$m and the wall about 1−3 nm) can be seen from the TEM images. The crystalline lattice distances in the white frame are 3.25 Å, corresponding to the (0019) plane of $In_2S_3$.

The FT-IR spectra of GO and $In_2S_3$/rGO NT composites were shown in Figure S4. In GO, three strong absorption peaks at 1050, 1740, and 3410 $cm^{-1}$ can be assigned to the C−O epoxide, carboxyl functional moieties, and O−H stretching vibration, respectively.[29,30] Moreover, the absorption peak at 1220 $cm^{-1}$ contributes from the C−O stretching vibrations of phenolic C−OH, while the absorption peak at 1620 $cm^{-1}$ might come from the skeletal vibrations of unoxidized C−C bonding or the H−O−H bending band of adsorbed $H_2O$ molecules.[31] In contrast, there were almost no C−O and O−H absorption bands in $In_2S_3$/rGO NT spectra, which implies that most of the oxygen containing groups were reduced.

To reveal the growth process of the $In_2S_3$/rGO NT, we investigated the relationship between sample phase, morphology, and synthetic time. From XRD patterns (Figure 3f), one can clearly find that 1 h is long enough for the formation of $In_2S_3$. However, note that no regular morphology at the initial stage (Figure 3a and Figure 3b) was found. By increase of the reaction time to 4 h, some particles with sizes around tens of nanometers were observed (Figure 3c). With continuing to prolong the reaction time to 10 h, some nanotubes started to appear; however, some nanoparticles still remained (Figure 3d and Figure 3e). With further prolonging of the reaction time to 24 h, all nanoparticles disappeared and all monodispersed and regular $In_2S_3$ NT structures could be clearly seen. Here, we believed that the reaction time is a deciding factor in the formation of $In_2S_3$/rGO NT. Meanwhile, through summarizing the experimental phenomena, we believed that the nanotube structures were formed by a rearrangement of the particles

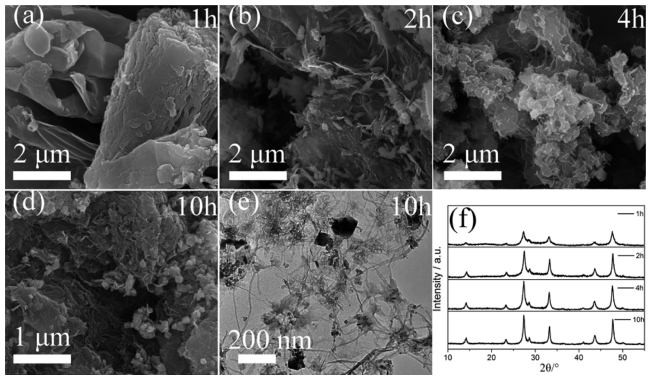


**Figure 3.** SEM images of the $In_2S_3$/rGO NT samples synthesized at 180 °C for (a) 1 h, (b) 2 h, (c) 4 h, (d) 10 h. (e) TEM image of $In_2S_3$/rGO NT sample synthesized at 180 °C for 10 h. (f) XRD patterns of the as-prepared sample.

aligned in the parallel direction and grew in a single direction in 1D growth by self-assembly.[10]

Additionally, several other experiments were measured to analyze the roles of the organic additives and templates in the formation of $In_2S_3$/rGO NT. No regular product was observed if TAA was replaced by thiourea or $Na_2S$ while the other experimental conditions remained unchanged (Figure S5a and Figure S5b). Furthermore, when no TAA was added to the reaction system, we obtained bulk $In_2S_3$/rGO (its SEM images, XPS and XRD patterns are shown in Figure S6 and Figure S7 in the Supporting Information, respectively). Meanwhile, if PVA was replaced by polyethylene glycol (PEG 400), irregular product was also produced (Figure S8). These phenomena mean that the sulfur source and templates are irreplaceable in forming the morphology of precursor NT during the calcination process.

CV was performed to investigate the catalytic activity of the as-prepared $In_2S_3$/rGO NT composite toward the reduction of $I_3^-$ (Figure 4). For Pt, two pairs of oxidation and reduction peaks were predominantly observed in two curves.

$$3I^- \rightarrow I_3^- + 2e \quad (1)$$

$$2I_3^- \rightarrow 3I_2 + 2e \quad (2)$$

$$3I_2 + 2e \rightarrow 2I_3^- \quad (3)$$

$$I_3^- + 2e \rightarrow 3I^- \quad (4)$$

According to the previous report, the relative positive pair is attributed to the process of oxidizing $I^-$ to $I_3^-$ (eq 1) and then to $I_2$ (eq 2). In the reverse process, $I_2$ is first reduced to $I_3^-$ (eq 3) and then to $I^-$ (eq 4).[32,33] Likewise, two pairs of oxidation and reduction peaks were appeared in $In_2S_3$/rGO NT, and the voltammogram had a perfect appearance, demonstrating that $In_2S_3$/rGO NT is also a satisfactory electrochemical catalyst. Note that, the $E_{pp}$ (peak-to-peak splitting) for $In_2S_3$/rGO NT (308 mV) was significantly smaller than Pt (502 mV). In theory, $E_{pp}$ varies inversely with the charge transfer rate and reversibility.[34,35] Thus, we can deduce that the charge transfer rate and reversibility for $In_2S_3$/rGO NT were better than Pt.

Subsequently, we introduced the $In_2S_3$-based samples into the DSCs system using the traditional $I^-/I_3^-$ electrolyte. Figure 5a shows the $J$−$V$ curves for DSCs using Pt, $In_2S_3$/rGO NT, bulk $In_2S_3$/rGO, and pure $In_2S_3$ (its SEM images, XPS and XRD patterns are shown in Figure S9 and Figure S10 in the Supporting Information, respectively) as CEs. As shown in


DOI: 10.1021/acsami.5b05519
ACS Appl. Mater. Interfaces 2015, 7, 20164−20169

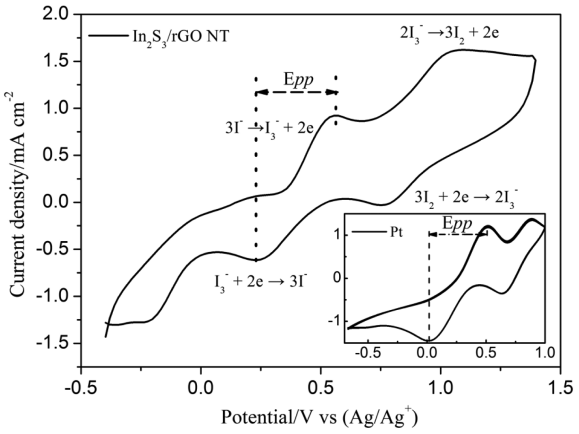


**Figure 4.** CV curves of the $I_3^-$ and $I^-$ redox couple for $In_2S_3$/rGO NT and Pt electrodes.

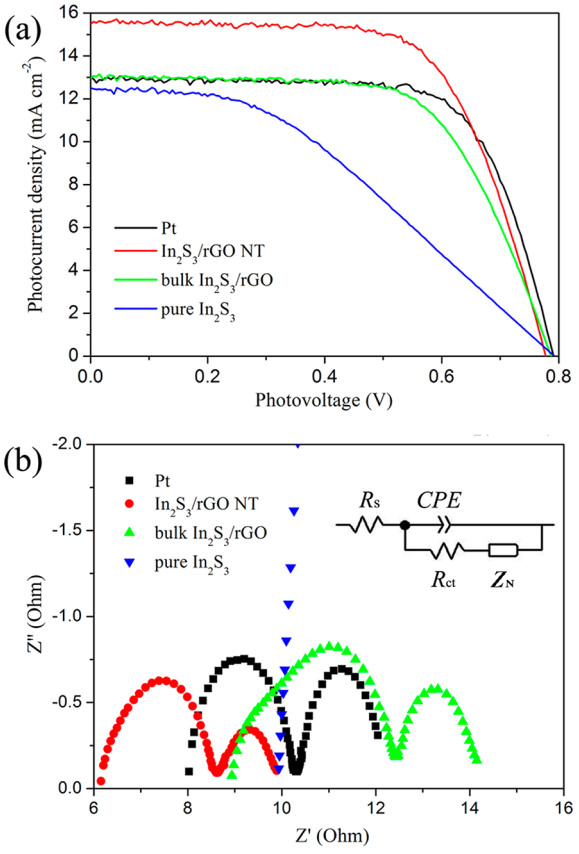


**Figure 5.** (a) Photocurrent–voltage curves of DSCs with four different CEs. (b) Impedance data of four different CEs and equivalent circuit diagram of the symmetrical cell.

Table 1, the DSCs with pure $In_2S_3$ and bulk $In_2S_3$/rGO as CEs showed $\eta$ of 3.86% and 6.62%, respectively. This means that the pure $In_2S_3$ and bulk $In_2S_3$/rGO CEs might not be efficient catalysts for DSCs. In contrast, when the $In_2S_3$/rGO NT CE was used, $\eta$ can go as high as 8.01%, which is significantly higher than that of the commercial Pt CE (7.18%). Besides $\eta$, the open-circuit voltage ($V_{oc}$) values, short-circuit current density ($J_{sc}$) values, and fill factor (FF) values are all improved significantly (Table 1). Thus, we believed that combining graphene and $In_2S_3$ NT structure configuration into a single unit can boost up $\eta$ in DSCs. To the best of our knowledge, this $In_2S_3$/rGO NT system has the best performance ever reported for $In_2S_3$-based CEs in the DSCs system.

Furthermore, the catalytic activity of $In_2S_3$/rGO NT was reconfirmed by EIS. Figure 5b shows the Nyquist plots of the symmetric cells (CE/electrolyte/CE) based on four kinds of CEs. In a Nyquist plot, the high-frequency (~100 MHz) intercept on the real axis represents series resistance ($R_s$). Two semicircles in the middle- and low-frequency regions can offer information on the charge-transfer resistance ($R_{ct}$) and the constant phase element of capacitance corresponding to $R_{ct}$ (CPE), and the diffusion resistance ($Z_N$) of the triiodide/iodide couple in the electrolyte, respectively.[36,37] Compared with pure $In_2S_3$ CE, bulk $In_2S_3$/rGO CE shows a much smaller $R_{ct}$ (3.55 Ω), which reveals that bulk $In_2S_3$/rGO materials can have better catalytic triiodide reduction behavior than pure $In_2S_3$.[38] We analyzed that the better catalytic ability to triiodide reduction and high diffusion velocity of triiodide may be due to introduction of graphene. Large surface area of graphene could capture electrons effectively. This will lead to redox couples ($I^-$/ $I_3^-$) being easily reduced in the electrolyte.[39] Meanwhile, smooth surface of graphene is helpful to the diffusion of triiodide.

When we changed $In_2S_3$ morphology from bulk to NT, we found that the catalytic performance of $In_2S_3$/rGO NT is significantly improved. It was worth noting that the performance trend does not track with the amount of $In_2S_3$/rGO catalyst present, as the typical mass loading of the pure bulk $In_2S_3$/rGO sample ($25 \pm 3$ mg cm$^{-2}$) is higher than that of the $In_2S_3$/rGO NT sample ($20 \pm 2$ mg cm$^{-2}$), which suggests that great electrocatalytic activity of $In_2S_3$/rGO NT should be due to its unique morphology structure. We observed that $In_2S_3$/rGO NT has a small $R_s$ value, indicating that the $In_2S_3$/rGO materials are firmly bonded to the substrate.[38] Flexible $In_2S_3$ NT structure could be very helpful to fill tubes in graphene wrinkles, making the whole material possess a smooth surface, which could further improve the bonding of the $In_2S_3$/rGO NT to the conductive substrate. This configuration is conducive to improving the capacity of electron transmission across the CE/substrate interface, with undoubted benefit to the improvement of catalytic performance. The $R_{ct}$ value of $In_2S_3$/rGO NT is 2.32 Ω, similar to the value of Pt (2.21 Ω). The most obvious difference between the $In_2S_3$/rGO NT and Pt is the $Z_N$ value. According to eq 5, $Z_N$ varies inversely with the diffusion coefficient of triiodide ($D$). Thus, small $Z_N$ of $In_2S_3$/rGO NT

**Table 1. Photovoltaic Parameters of the DSCs Using Four Kinds of CEs and EIS Parameters of the Dummy Cells Based on Four Electrodes**

| CE | $V_{oc}$ (V) | $J_{sc}$ (mA cm$^{-2}$) | FF | $\eta$ (%) | $R_s$ (Ω) | $R_{ct}$ (Ω) | CPE | $Z_N$ (Ω) |
|---|---|---|---|---|---|---|---|---|
| Pt | 0.80 | 12.98 | 0.69 | 7.18 | 8.00 | 2.21 | 0.80 | 1.85 |
| $In_2S_3$/rGO NT | 0.78 | 15.48 | 0.66 | 8.01 | 6.22 | 2.32 | 0.76 | 1.27 |
| bulk $In_2S_3$/rGO | 0.79 | 12.95 | 0.65 | 6.62 | 8.95 | 3.55 | 0.63 | 1.46 |
| pure $In_2S_3$ | 0.79 | 12.50 | 0.39 | 3.86 | 9.78 | 38.26 | 0.90 | 2.01 |


DOI: 10.1021/acsami.5b05519
ACS Appl. Mater. Interfaces 2015, 7, 20164–20169

means a high diffusion velocity of triiodide. This factor is obviously beneficial to regeneration of $I^-$, which then continues to promote the regeneration of the sensitizer.[40] In this system, although $In_2S_3$/rGO NT and Pt exhibited closed $R_{ct}$ values, the small $Z_N$ of $In_2S_3$/rGO NT was a main factor in obtaining an excellent catalytic performance.[41] Of course, smaller $Z_N$ value leads to $J_{sc}$ for the corresponding DSCs. In short, the combined actions of $R_{ct}$ and $Z_N$ were responsible for the high $\eta$ of $In_2S_3$/rGO NT.

$$Z_N = \frac{W}{\sqrt{i\omega}} \tanh\left(\sqrt{\frac{i\omega}{K_N}}\right) \quad (5)$$

where $W = kT/(n^2e^2CAD^{1/2})$, $K_N = D/\delta^2$, $k$ is the Boltzmann constant, $n$ is the number of electrons transferred in the reaction, $e$ is the elementary charge, $C$ is the concentration of triiodide, $D$ is the diffusion coefficient of triiodide, and $\delta$ is the thickness of the diffusion layer.

In fact, the catalyst superiority of the $In_2S_3$/rGO NT over the bulk $In_2S_3$/rGO is easily understood. On irregular bulk surfaces, the electrons or holes must move through many interfaces before they can recombine with each other. This will lead to a decline in electrocatalytic activity of bulk $In_2S_3$/rGO.[42,43] In contrast, circular arc surface structure of NT greatly reduces the electronic mobile obstacles, which is helpful to reduce the waste of catalytic ability. On the other hand, because of the hollow framework, 1D NT possesses great flexibility, and this feature would effectively prevent aggregation and therefore maintain a large active surface area.

## CONCLUSIONS

In summary, a novel $In_2S_3$/rGO NT composite has been successfully synthesized through hydrothermal conditions by employing $InCl_3$ and thioacetamide as In and S sources and PVA as a template. During synthesis, we found that the sulfur source and templates play key roles in determining the morphology and structure of the final products. The as-fabricated $In_2S_3$/rGO NT composite showed a remarkable electrocatalytic activity toward the iodide species reduction reaction. Importantly, when evaluated as potential CE materials for DSCs, the $In_2S_3$/rGO composite with unique NT structure exhibited high energy conversion efficiency.

## ASSOCIATED CONTENT

### Supporting Information

The Supporting Information is available free of charge on the ACS Publications website at DOI: 10.1021/acsami.5b05519.

Figure S1 showing the AFM images of GO powder, Figure S2 showing the XPS images of $In_2S_3$/rGO NT sample, Figure S3 showing the FE-SEM images of $In_2S_3$/rGO NT sample, Figure S4 revealing the FT-IR images of $In_2S_3$/rGO NT sample, Figure S5 showing the SEM images of sample synthesized by different sulfur sources, Figure S6 showing the SEM images of bulk $In_2S_3$/rGO sample, Figure S7 showing the XPS and XRD pattern of bulk $In_2S_3$/rGO sample, Figure S8 showing the SEM image of sample synthesized by PEG 400 as template, Figure S9 showing the SEM images of pure $In_2S_3$ sample, and Figure S10 showing the XPS and XRD patterns of pure $In_2S_3$ sample (PDF)

## AUTHOR INFORMATION


### Corresponding Authors

*F.-z.H.: e-mail, fzhu@nankai.edu.cn.
*Q.-c.Z.: e-mail, qczhang@ntu.edu.sg.
*L.L.: e-mail, liul@nankai.edu.cn.


### Notes

The authors declare no competing financial interest.

## ACKNOWLEDGMENTS

This work was supported by the National Natural Science Foundation of China (Grant 21271108), the Ministry of Science and Technology (Grant 2014CB932001), 2011 Natural Science Foundation of Tianjin (Grant 11JCZDJC24800), and China-U.S. Center for Environmental Remediation and Sustainable Development. Q.-c.Z. acknowledges financial support from the Singapore Ministry of Education through AcRF Tier 1 (Grant RG 16/12) and Tier 2 (Grants ARC 20/a2 and 2/13) and from the National Research Foundation CREATE program (Nanomaterials for Energy and Water Man-agement).

## REFERENCES


(1) Lucena, R.; Aguilera, I.; Palacios, P.; Wahnón, P.; Conesa, J. C. Synthesis and Spectral Properties of Nanocrystalline V-Substituted $In_2S_3$, a Novel Material for More Efficient Use of Solar Radiation. *Chem. Mater.* **2008**, *20*, 5125−5127.

(2) Park, K. H.; Jang, K.; Son, S. U. Synthesis, Optical Properties, and Self-Assembly of Ultrathin Hexagonal $In_2S_3$ Nanoplates. *Angew. Chem., Int. Ed.* **2006**, *45*, 4608−4612.

(3) Qiu, W. M.; Xu, M. S.; Yang, X.; Chen, F.; Nan, Y. X.; Zhang, J. L.; Iwai, H.; Chen, H. Z. Biomolecule-Assisted Hydrothermal Synthesis of $In_2S_3$ Porous Films and Enhanced Photocatalytic Properties. *J. Mater. Chem.* **2011**, *21*, 13327−13333.

(4) Du, W. M.; Zhu, J.; Li, S. X.; Qian, X. F. Ultrathin $\beta$-$In_2S_3$ Nanobelts: Shape-Controlled Synthesis and Optical and Photocatalytic Properties. *Cryst. Growth Des.* **2008**, *8*, 2130−2136.

(5) Datta, A.; Sinha, G.; Panda, S. K.; Patra, A. Growth, Optical, and Electrical Properties of $In_2S_3$ Zigzag Nanowires. *Cryst. Growth Des.* **2009**, *9*, 427−431.

(6) Yang, M. Q.; Weng, B.; Xu, Y. J. Synthesis of $In_2S_3$−CNT Nanocomposites for Selective Reduction under Visible Light. *J. Mater. Chem. A* **2014**, *2*, 1710−1720.

(7) Chen, L. Y.; Zhang, Z. D.; Wang, W. Z. Self-Assembled Porous 3D Flowerlike-$In_2S_3$ Structures: Synthesis, Characterization, and Optical Properties. *J. Phys. Chem. C* **2008**, *112*, 4117−4123.

(8) Liu, L.; Liu, H. J.; Kou, H. Z.; Wang, Y. Q.; Zhou, Z.; Ren, M. M.; Ge, M.; He, X. W. Morphology Control of $\beta$-$In_2S_3$ from Chrysanthemum-Like Microspheres to Hollow Microspheres: Synthesis and Electrochemical Properties. *Cryst. Growth Des.* **2009**, *9*, 113−117.

(9) Rengaraj, S.; Venkataraj, S.; Tai, C.-W.; Kim, Y.; Repo, E.; Sillanpää, M. Self-Assembled Mesoporous Hierarchical-like $In_2S_3$ Hollow Microspheres Composed of Nanofibers and Nanosheets and Their Photocatalytic Activity. *Langmuir* **2011**, *27*, 5534−5541.

(10) Kim, Y. H.; Lee, J. H.; Shin, D.-W.; Park, S. M.; Moon, J. S.; Nam, J. G.; Yoo, J.-B. Synthesis of Shape-Controlledb-$In_2S_3$ Nanotubes through Oriented Attachment of Nanoparticles. *Chem. Commun.* **2010**, *46*, 2292−2294.

(11) Liu, G. D.; Jiao, X. L.; Qin, Z. H.; Chen, D. R. Solvothermal Preparation and Visible Photocatalytic Activity of Polycrystalline $\beta$-$In_2S_3$ Nanotubes. *CrystEngComm* **2011**, *13*, 182−187.

(12) So, S.; Hwang, I.; Schmuki, P. Hierarchical DSSC Structures based on "Single Walled" $TiO_2$ Nanotube Arrays Reach a Back-Side Illumination Solar Light Conversion Efficiency of 8%. *Energy Environ. Sci.* **2015**, *8*, 849−854.




DOI: 10.1021/acsami.5b05519
*ACS Appl. Mater. Interfaces* 2015, 7, 20164−20169

(13) Roy-Mayhew, J. D.; Aksay, I. A. Graphene Materials and Their Use in Dye-Sensitized Solar Cells. *Chem. Rev.* **2014**, *114*, 6323−6348.
(14) Geim, A. Graphene: Status and Prospects. *Science* **2009**, *324*, 1530−1534.
(15) Park, S.; Ruoff, R. Chemical Methods for the Production of Graphenes. *Nat. Nanotechnol.* **2009**, *4*, 217−224.
(16) Wu, J.; Pisula, W.; Müllen, K. Graphene as Potential Material for Electronics. *Chem. Rev.* **2007**, *107*, 718−747.
(17) Ju, M. J.; Jeon, I.-Y.; Kim, J. C.; Lim, K.; Choi, H.-J.; Jung, S.-M.; Choi, I. T.; Eom, Y. K.; Kwon, Y. J.; Ko, J.; Lee, J.-J.; Kim, H. K.; Baek, J.-B. Graphene Nanoplatelets Doped with N at its Edges as Metal-Free Cathodes for Organic Dye-Sensitized Solar Cells. *Adv. Mater.* **2014**, *26*, 3055−3062.
(18) Liu, J. L.; Zhang, L. L.; Wu, H. B.; Lin, J. Y.; Shen, Z. X.; Lou, X. W. High-Performance Flexible Asymmetric Super Capacitors Based on a New Graphene Foam/Carbon Nanotube Hybrid Film. *Energy Environ. Sci.* **2014**, *7*, 3709−3719.
(19) Peng, C. X.; Chen, B. D.; Qin, Y.; Yang, S. H.; Li, C. Z.; Zuo, Y. H.; Liu, S. Y.; Yang, J. H. Facile Ultrasonic Synthesis of CoO Quantum Dot/Graphene Nanosheet Composites with High Lithium Storage Capacity. *ACS Nano* **2012**, *6*, 1074−1082.
(20) Gao, G. X.; Wu, H. B.; Lou, X. W. Citrate-Assisted Growth of $NiCo_2O_4$ Nanosheets on Reduced Graphene Oxide for Highly Reversible Lithium Storage. *Adv. Energy Mater.* **2014**, *4*, 1400422.
(21) Perera, S. D.; Mariano, R. G.; Vu, K.; Nour, N.; Seitz, O.; Chabal, Y.; Balkus, K. J. Hydrothermal Synthesis of Graphene-$TiO_2$ Nanotube Composites with Enhanced Photocatalytic Activity. *ACS Catal.* **2012**, *2*, 949−956.
(22) Ye, F. M.; Du, G. H.; Jiang, Z. F.; Zhong, Y. J.; Wang, X. D.; Cao, Q. P.; Jiang, J. Z. Facile and Rapid Synthesis of RGO−$In_2S_3$ Composites with Enhanced Cyclability and High Capacity for Lithium Storage. *Nanoscale* **2012**, *4*, 7354−7357.
(23) Yang, M. Q.; Weng, B.; Xu, Y. J. Improving the Visible Light Photoactivity of $In_2S_3$−Graphene Nanocomposite via a Simple Surface Charge Modification Approach. *Langmuir* **2013**, *29*, 10549−10558.
(24) Yang, X.; Chan, C. Y.; Xue, H. T.; Xu, J.; Tang, Y. B.; Wang, Q.; Wong, T. L.; Lee, C. S. One-Pot Synthesis of Graphene/$In_2S_3$ Nanoparticle Composites for Stable Rechargeable Lithium Ion Battery. *CrystEngComm* **2013**, *15*, 6578−6584.
(25) Kotov, N. A. Materials Science: Carbon Sheet Solutions. *Nature* **2006**, *442*, 254−255.
(26) O'Regan, B.; Grätzel, M. A Low-Cost, High-Efficiency Solar Cell Based on Dye-Sensitized Colloidal $TiO_2$ Film. *Nature* **1991**, *353*, 737−740.
(27) Murakami, T. N.; Grätzel, M. Counter Electrodes for DSC: Application of Functional Materials as Catalysts. *Inorg. Chim. Acta* **2008**, *361*, 572−580.
(28) Chai, B.; Zeng, P.; Zhang, X. H.; Mao, J.; Zan, L.; Peng, T. Y. Walnut-Like $In_2S_3$ Microspheres: Ionic Liquid-Assisted Solvothermal Synthesis, Characterization and Formation Mechanism. *Nanoscale* **2012**, *4*, 2372−2377.
(29) Guo, H. L.; Wang, X. F.; Qian, Q. Y.; Wang, F. B.; Xia, X. H. A Green Approach to the Synthesis of Graphene Nanosheets. *ACS Nano* **2009**, *3*, 2653−2659.
(30) Szabó, T.; Tombácz, E.; Illés, E.; Dékány, I. Enhanced Acidity and pH-Dependent Surface Charge Characterization of Successively Oxidized Graphite Oxides. *Carbon* **2006**, *44*, 537−545.
(31) Nethravathi, C.; Rajamathi, M. Chemically Modified Graphene Sheets Produced by the Solvothermal Reduction of Colloidal Dispersions of Graphite Oxide. *Carbon* **2008**, *46*, 1994−1998.
(32) Chang, S.-H.; Lu, M.-D.; Tung, Y.-L.; Tuan, H.-Y. Gram-Scale Synthesis of Catalytic $Co_9S_8$ Nanocrystal Ink as a Cathode Material for Spray-Deposited, Large Area Dye-Sensitized Solar Cells. *ACS Nano* **2013**, *7*, 9443−9451.
(33) Popov, A. I.; Geske, D. H. Studies on the Chemistry of Halogen and of Polyhalides. XIII. Voltammetry of Iodine Species in Acetonitrile. *J. Am. Chem. Soc.* **1958**, *80*, 1340−1341.
(34) Roy-Mayhew, J. D.; Bozym, D. J.; Punckt, C.; Aksay, I. A. Functionalized Graphene as a Catalytic Counter Electrode in Dye-Sensitized Solar Cells. *ACS Nano* **2010**, *4*, 6203−6211.
(35) Nicholson, R. S. Theory and Application of Cyclic Voltammetry for Measurement of Electrode Reaction Kinetics. *Anal. Chem.* **1965**, *37*, 1351−1355.
(36) Wu, M. X.; Lin, X.; Wang, Y.; Wang, L.; Guo, W.; Qi, D.; Peng, X.; Hagfeldt, A.; Grätzel, M.; Ma, T. L. Economical Pt-Free Catalysts for Counter Electrodes of Dye-Sensitized Solar Cells. *J. Am. Chem. Soc.* **2012**, *134*, 3419−3428.
(37) Miao, X. H.; Pan, K.; Wang, G. F.; Liao, Y. P.; Wang, L.; Zhou, W.; Jiang, B. J.; Pan, Q. J.; Tian, G. H. Well-Dispersed CoS Nanoparticles on a Functionalized Graphene Nanosheet Surface: a Counter Electrode of Dye-Sensitized Solar Cells. *Chem. - Eur. J.* **2014**, *20*, 474−482.
(38) Wu, M. X.; Lin, X.; Hagfeldt, A.; Ma, T. L. Low-Cost Molybdenum Carbide and Tungsten Carbide Counter Electrodes for Dye-Sensitized Solar Cells. *Angew. Chem., Int. Ed.* **2011**, *50*, 3520−3524.
(39) Hauch, A.; Georg, A. Diffusion in the Electrolyte and Charge-Transfer Reaction at the Platinum Electrode in Dye-Sensitized Solar Cells. *Electrochim. Acta* **2001**, *46*, 3457−3466.
(40) Guo, S. Q.; Jing, T. Z.; Zhang, X.; Yang, X. B.; Yuan, Z. H.; Hu, F. Z. Mesoporous $Bi_2S_3$ Nanorods with Graphene-Assistance as Low-Cost Counter-Electrode Materials in Dye-Sensitized Solar Cells. *Nanoscale* **2014**, *6*, 14433−14440.
(41) Wu, M. X.; Wang, Y. D.; Lin, X.; Yu, N. S.; Wang, L.; Wang, L. L.; Hagfeldt, A.; Ma, T. L. Economical and Effective Sulfide Catalysts for Dye-Sensitized Solar Cells as Counter Electrodes. *Phys. Chem. Chem. Phys.* **2011**, *13*, 19298−19301.
(42) Wang, Y. C.; Wang, D. Y.; Jiang, Y. T.; Chen, H. A.; Chen, C. C.; Ho, K. C.; Chou, H. L.; Chen, C. W. $FeS_2$ Nanocrystal Ink as a Catalytic Electrode for Dye-Sensitized Solar Cells. *Angew. Chem., Int. Ed.* **2013**, *52*, 6694−6698.
(43) Wang, W. J.; Pan, X.; Liu, W. Q.; Zhang, B.; Chen, H. W.; Fang, X. Q.; Yao, J. X.; Dai, S. Y. $FeSe_2$ Films with Controllable Morphologies as Efficient Counter Electrodes for Dye-Sensitized Solar Cells. *Chem. Commun.* **2014**, *50*, 2618−2620.


DOI: 10.1021/acsami.5b05519
*ACS Appl. Mater. Interfaces* 2015, 7, 20164−20169